J. Fluid Mech. (1998), *vol.* 354, *pp.* 101–121. Printed in the United Kingdom

Turbulent convection into a linearly stratified fluid: the generation of 'subsurface anticyclones'

By SIAVASH NARIMOUSA

University of Southern California, Department of Mechanical Engineering,
Los Angeles, CA 90089-1453, USA

(Received 27 July 1996 and in revised form 4 August 1997)

Penetrative turbulent convection from a localized circular top source into a rotating, linearly stratified ambient fluid of strength N has been investigated in a laboratory tank. Initially, the induced three-dimensional convective flow penetrated rapidly into the stratified water column until it reached an equilibrium depth at which the convective flow began to propagate radially outward. At this stage, the usual cyclonic vortices were generated around the convection source at the edge of the radially propagating flow. Soon after, a thin 'subsurface anticyclone' was formed at the level of equilibrium depth beneath the convection source. Later, this anticyclone dominated the central part of the convective regime and did not allow new cyclones to be injected into the system. After reaching its maximum mean diameter $D_a/R \approx 10(R_{0,R})^{2/3}$ and swirl velocity $v_a \approx (B_0R)^{1/3}$, an anticyclone became unstable and split into two new vortices that left the area beneath the source, allowing a new anticyclone to form at its original place (here, $R_{0,R} = (B_0/f^3R^2)^{1/2}$ is the Rossby number based on R the radius of the source, B_0 is the surface negative buoyancy flux, and f is the Coriolis parameter). These observations provide crucial evidence that many of the 'subsurface anticyclonic' vortices detected in the stratified pycnocline of the central Arctic Ocean are indeed generated as a result of convective processes occurring in this region.

1. Introduction

It is well known that intense cooling and/or freezing of the ocean surface and seas results in a turbulent convection that can penetrate deep into the water column. Field observations have revealed vigorous convection in the Greenland Sea (Gascard 1978; Schott, Visbeck & Send 1993), Labrador Sea (Lazier 1980) and Gulfe du Lions south of France (Schott & Leaman 1991; MEDOC Group 1970). It is reported that before the onset of such convection the water columns in the Greenland Sea and Gulfe du Lions (Gascard 1991), the Labrador Sea (Lazier 1994) and the upper stratified layer (pycnocline) of the central Arctic Ocean (Hunkins 1974; Newton, Aagaard & Coachman 1974) are linearly stratified. Also, a great number of mesoscale vortices (more than a hundred) with a mean diameter of about 10–20 km and maximum velocity of about 30 cm s^{-1} have been detected within the pycnocline of the central Arctic Ocean (Newton *et al.* 1974; Hunkins 1974; Manley & Hunkins 1985; D'Asaro 1988). The majority of these vortices have been reported to be anticyclonic and to last for a long time. Hart & Killworth (1976) have suggested that the generation of such vortices may arise from instability of the basic stratification in shallow regions. D'Asaro (1988) has proposed that the flow separation at Barrow Canyon is a likely source for the generation of many of these vortices. Maxworthy & Narimousa (1994), Narimousa (1996) and Jones & Marshall (1993) demonstrated via laboratory and numerical modelling that many of these vortices arise from baroclinic instability of the convective system itself. Unlike the observed anticyclonic vortices of the Arctic, the vast majority of the laboratory vortices generated in homogeneous and two-layer stratified ambient fluid are of cyclonic type. Although these models provide valuable information on the dynamics of the convective systems, they have not explained the anticyclonic behaviour of the vortices detected in the upper layer of the central Arctic Ocean. In the present paper, a study of turbulent convection in linearly stratified ambient fluid is carried out which demonstrates new evidence for the formation and dynamics of the 'subsurface anticyclonic' vortices generated in such convective systems and the upper layer of the central Arctic Ocean.

To achieve our objectives, we employed the same laboratory model as in Narimousa (1996) to study convection in linearly stratified ambient fluid. The first laboratory modelling of this type of convection was conducted by Ivey, Taylor & Coates (1995) and Coates, Ivey & Taylor (1995) who studied rotating convection driven by a heat source in a thermally linearly stratified ambient fluid. In our experiments salt water is used to produce linear stratification and to generate a negative buoyancy force to activate a deep convective process. For both cases (heat and salt), the initial conditions are chosen so that the convective flow beneath the convection source is three-dimensional turbulent and reaches an equilbrium depth h_e. At this depth, the flow begins to propagate radially to allow mesoscale vortices to form at the edge of the propagating front around the source. The equilbrium depth h_e can be used to define a common Rossby number $R_0^* = (B_0/f^3h_e^2)^{1/2}$ (where B_0 is the surface negative buoyancy flux and f is the Coriolis parameter), similar to the one introduced by Maxworthy & Narimousa (1991, 1994) for such convective systems. Using the Rossby number R_0^*, we find that the present experiments have been conducted at higher values of R_0^* ($0.09 \leqslant R_0^* \leqslant 3.44$) than those of Ivey *et al.* (1995) and Coates *et al.* (1995) which were conducted at values of $R_0^* \leqslant 0.2$. Also, we have shown that the molecular effect due to use of salt or heat (Narimousa 1997) is negligible when estimating the gross properties of a convective system at high Rayleigh number $R_a = (B_0H^4)/(\kappa^2 \nu)$, where H is the depth of the fluid layer, ν is the kinematic viscosity and κ is the molecular diffusivity of salt and/or heat. In the light of this, the present work can be considered as an extension of the Ivey *et al.* (1995) and Coates *et al.* (1995) experiments, with higher values of R_0^* and R_a.

Most recently, Visbeck, Marshall & Jones (1996) reported the first numerical simulation of deep convection in a linearly stratified water column. Their model found that a scaling argument also predicted that the convective flow will reach an equilibrium depth given by $h_e \sim (B_0R)^{1/3}/N$, which is however different from that $h_e \sim (B_0t)^{1/2}/N$ given by Ivey *et al.* (1995) and Coates *et al.* (1995) (here t is time). Recent laboratory experiments by Whitehead, Marshall & Hufford (1996) focused on the measurements of h_e and found $h_e \sim 4.6(B_0R)^{1/3}/N$, in agreement with that given by Visbeck *et al.* (1996). In the present experiments we will also examine the validity of the above relationships for h_e.

Narimousa (1996) has studied turbulent convection into a two-layer stratified ambient fluid where penetrative convective flow interacted with a density interface. It has been found that the Richardson number $Ri = (g_i'h_0)/(B_0R)^{2/3}$ of the system is a major factor for predicting the condition under which the convective flow penetrates the density interface. Here, h_0 is the depth of the top layer, g_i' is the reduced gravity between the two layers, and $(B_0R)^{1/3}$ is the velocity of the outflow from under the source (Phillips 1966). When $Ri > 11$, the convective flow will not penetrate the density

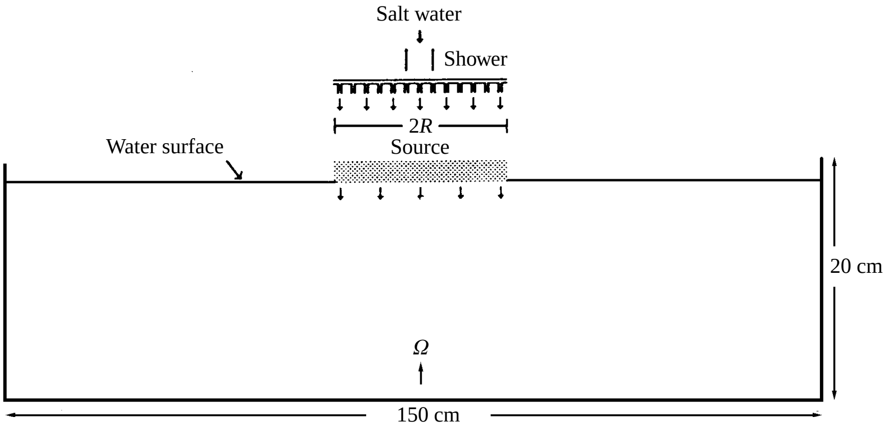

FIGURE 1. Schematic diagram of the side view of the experimental tank and its various components.

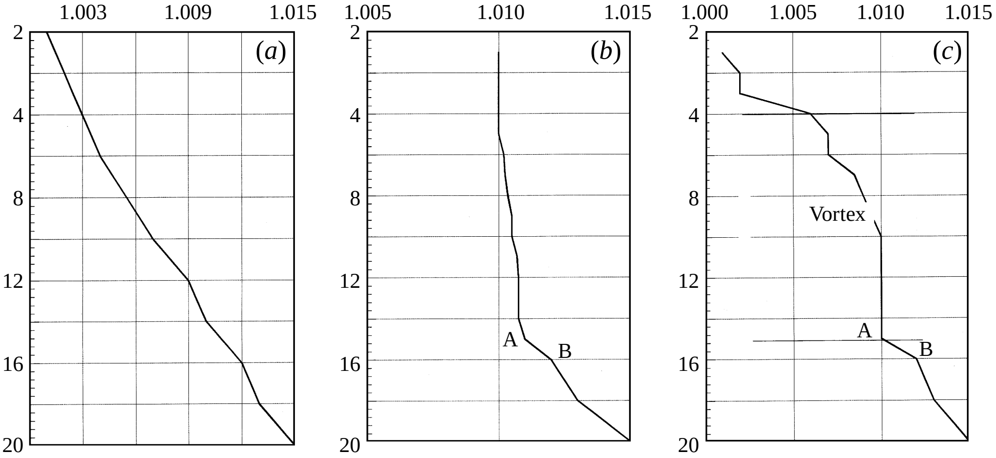

FIGURE 2. (a) Vertical density profile of a linearly stratified water column in a rotating system before the onset of convection for the experiment with $N \approx 0.83$ s^{-1}, $f \approx 1.0$ s^{-1}, $B_0 \approx 2.2$ cm^2 s^{-3} and $H \approx 20$ cm. (b) Vertical variation of density in the convective mixed layer beneath the source after the experiment (a) was subjected to the onset of deep convection and reached an equilibrium depth. (c) Vertical variation of density in a vortex column generated away from the source. Also, notice the presence of a weak density jump between points A and B on (b) and (c). Note that these measurements were taken by a transverse conductivity probe.

interface, while for values of $Ri < 11$ the convective flow will penetrate through the interface into the bottom layer. Consequently, when the convective flow reaches an equilibrium depth h_e in the present linear stratified experiments, the associated value of the Richardson number $Ri_e = (g_i' h_e)/(B_0 R)^{2/3}$ should be greater than 11. In §4, this critical value of the Richardson number will be employed to predict and estimate various components of the convective flow induced in the present study.

2. The experiment

The laboratory experiments were conducted in a large Plexiglas cylindrical tank 150 cm in diameter and 30 cm deep which was mounted on a turntable (figure 1). The tank was filled with linear stratified salt water (figure 2a) in such a way that the top surface of the water layer was in contact with the bottom of a circular convection source of radius ($R = 12.5$ cm). The source, located at the centre of the tank, consisted of a circular screen (with a mesh size of about 1 mm, and radius of about 12.5 cm) at its base, topped by filter paper and several layers of sponge. The system is brought to a solid-body rotation at a rate Ω (counter-clockwise looking from above) by a computer which was programmed to gradually increase the tank rotation rate from rest via a stepping motor. Depending upon the tank rotation rate Ω, it usually took about 24–48 h to bring an experimental setup into a solid-body rotation. When a rotation rate Ω was achieved, the convection source was activated to release denser salt water into the top surface of the stratified layer. Thereafter, the source water sank into the stratified water column beneath the source. In this way a growing three-dimensional turbulent convective flow was formed and penetrated rapidly into the water column (for details see §3).

In order to observe and measure the fluid motion throughout the test regions, both small neutrally buoyant particles (1 mm in diameter) and dye (fluorescein) were used. To illuminate the particles and/or dyed fluid horizontal and vertical sheets of lights were used separately. This enabled us to visualize the horizontal and the vertical structure of the convective regimes (see §3). As in Maxworthy & Narimousa (1994) the sense of rotation of cyclonic and anticyclonic vortices is revealed by direct observation: dye (figures 4 and 5) and pointed streak (that is, the particle shows the initial position and its tail shows the direction of the motion) photography (figure 6).

The initial density stratification was measured in two ways, using either a calibrated refractometer or a calibrated conductivity probe. Using the refractometer, before the system was set to rotate we measured the water density at depths 1 cm apart from top to bottom of the stratified layer ($H = 20$ cm). The conductivity probe, while travelling vertically downward, also measured the density of the water column (figure 2*a*). After these measurements, we brought the system to solid-body rotation and used a conductivity probe to repeat the density measurements. This assured us that when the system reached solid-body rotation its stratification remained unchanged. The above procedure enabled us to use the conductivity probe to measure the density of the convective flow at various locations during the running of an experiment (figure 2*b, c*).

The quantities under our control were the depth of the fluid layer (H), the rotation rate $\Omega = f/2\,\mathrm{s}^{-1}$, the buoyancy frequency of the stratified layer $N = \left(g/\rho_a\left(\delta\rho/\delta h\right)\right)^{1/2}$, the density of the source fluid above ambient $\delta\rho_s$, and its flow rate per unit area Q cm^3 s^{-1} (here, g is the acceleration due to gravity, ρ_a the average density of the ambient fluid, $\delta\rho$ the density difference across the depth of the stratified layer, and $\delta h = H$). The latter two quantities can be combined into one parameter, the buoyancy flux, $B_0 = Qg\delta\rho_s/4\pi\rho_a R^2$ cm^2 s^{-3}. The experimental parameters took the values: $0.96 \leqslant B_0 \leqslant 2.2\,\mathrm{cm}^2\,\mathrm{s}^{-3}$, $0.1 \leqslant f \leqslant 1.14\,\mathrm{s}^{-1}, 0.77 \leqslant N \leqslant 1.1\,\mathrm{s}^{-1}$ with the resulting ranges of values $0.09 \leqslant R_0^* \leqslant 3.44$, $0.09 \leqslant R_{0,R} \leqslant 1.27$ and $1 \leqslant N/f \leqslant 7.7$.

3. Experimental observations and description

3.1. *The initial deepening*

When a system was in solid-body rotation, the convection source was activated to allow denser salt water to sink into the top surface of the stratified water column beneath the source. As a result, a growing three-dimensional turbulent layer was

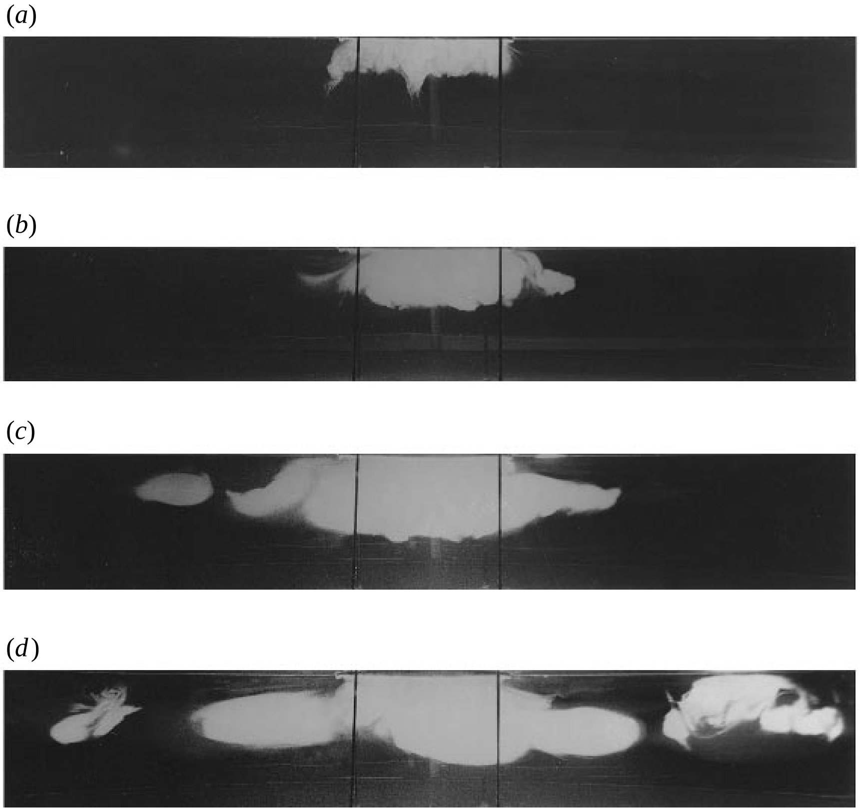

FIGURE 3. Successive vertical structures of the convective region revealed by dye and a vertical light slice through the centre of the tank for the experiment with with $N \approx 1.1\ \mathrm{s}^{-1}$, $f \approx 1.0\ \mathrm{s}^{-1}$, $B_0 \approx 1.98\ \mathrm{cm}^2\,\mathrm{s}^{-3}$ and $R_0^* \approx 0.12$. (*a*) At $T' = t/T \approx 1.5$ (where t is the time from the initiation of convection and $T = 4\pi/f$), showing the formation of a penetrative turbulent convective layer beneath the source. (*b*) At $T \approx 4.5$, showing that the convective flow has penetrated deeper into the stratified layer. (*c*) At $T' \approx 10$: the convective layer has reached its equilibrium depth h_e and has propagated radially outward. At this stage cyclonic vortices are seen to form at the edge of the propagating front. (*d*) At $T' \approx 16$, showing the formation of a well-developed convective system in a linearly stratified ambient fluid. Here, two cyclones are present at both ends of the convective flow. There are two more vortices that are attached to the convective flow beneath the source which could have anticyclonic circulation (see figure 8).

formed which then penetrated the linear stratification rapidly (see figure 3*a*). After reaching an equilibrium depth h_e (also called maximum depth, Ivey *et al.* 1995, and/or final depth, Visbeck *et al.* (1996)), the vertical penetration ceased and the convective flow began to propagate radially (horizontally) outward in the form of a gravity front (figures 3*b* and 4*a*). This front then underwent a baroclinic instability and eventually mesoscale cyclonic vortices were seen to form (see figures 3*c*, 4*b*, and 4*c*) at the edge of the front (see also Coates *et al.* 1995; Visbeck *et al.* 1996; Whitehead *et al.* 1996). Initially, the number of cyclonic vortices generated depends on the natural Rossby number $R_0^* = (B_0/f^3h_e^2)^{1/2}$ of the convective system (note that in a given experiment R_0^* is constant because h_e is constant, see §4.1). Figure 5 shows that the number of cyclonic vortices initially generated increases with decreasing R_0^*, while their mean diameter D decreases with decreasing R_0^*. These observations are similar to our previous observations in homogeneous cases at large R_0^* (Maxworthy & Narimousa

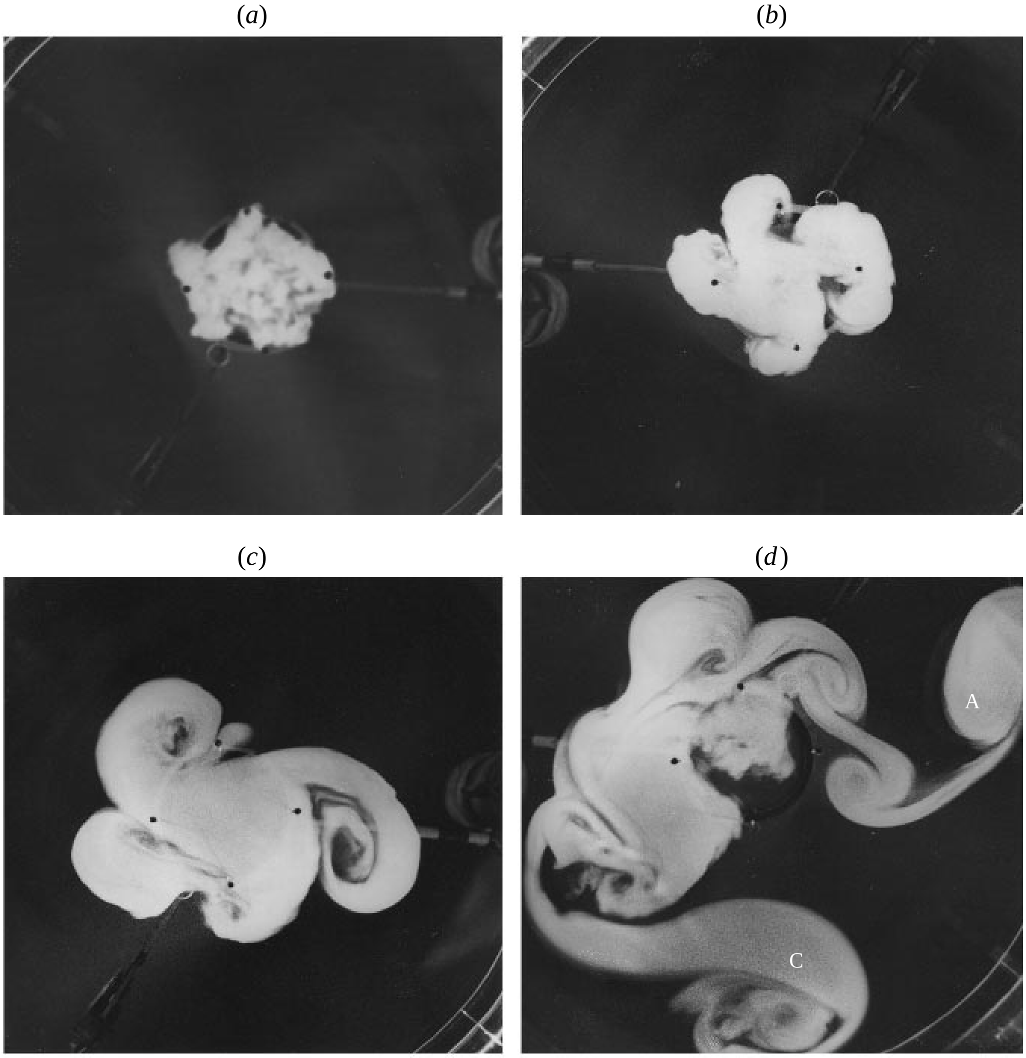

FIGURE 4. Successive horizontal structures of the convective regions revealed by dye and a horizontal light slice at about the base of the convective flow for the experiment with $N \approx 0.86\ \mathrm{s}^{-1}$, $f \approx 1.0\ \mathrm{s}^{-1}$, $B_0 \approx 2.2\ \mathrm{cm}^2\,\mathrm{s}^{-3}$ and $R_0^* \approx 0.1$. (*a*) At $T' \approx 2$: the base of the convective flow is at about the equilibrium depth. (*b*) At $T' \approx 3.5$, show the initial formation of four cyclonic vortices. (*c*) At $T' \approx 7$: the cyclonic vortices are well developed. (*d*) At $T' \approx 12$:, the well-organized cyclonic vortex field no longer exists and, surprisingly, one can observe at least one anticyclone (A) in the system.

1994; Narimousa 1997), and two-layer cases for when $Ri > 11$ (Narimousa 1996). In those experiments we have shown that the well-organized cyclonic vortices, eventually propagate away from the convection source allowing a new generation of cyclonic vortices to form in the vicinity of the source. This process will continue to repeat itself for as long as the convection source is active.

However, in the present case the situation is quite different because, as shown in figure 4(*d*), the well-organized cyclonic vortices of figure 4(*c*) are totally distorted. It can be seen that one of the cyclones (C) has been forced to propagate rather rapidly toward the wall of the tank, and the well-organized cyclonic vortex field near

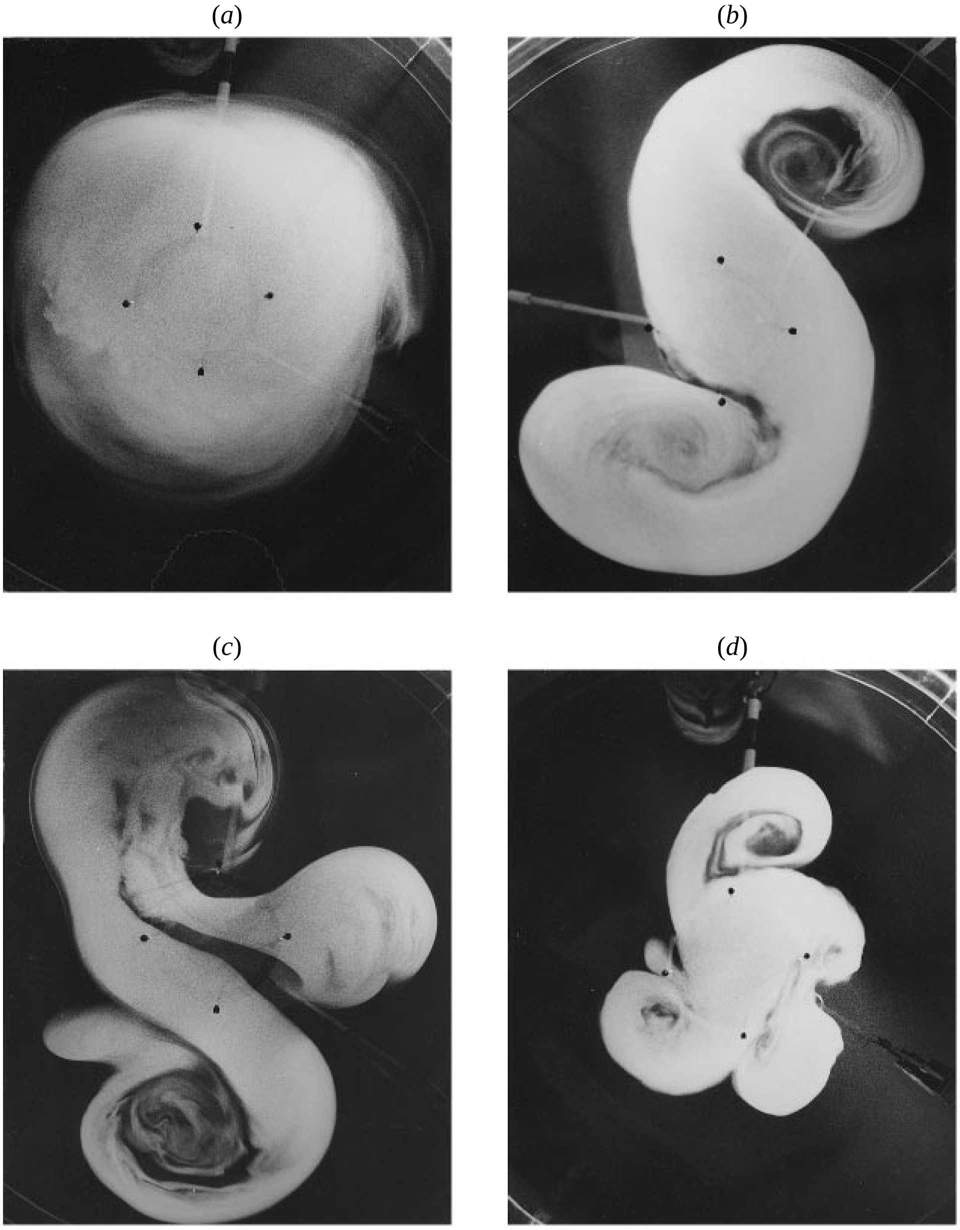

(*a*) (*b*) (*c*) (*d*)

FIGURE 5. Horizontal structures of the convective vortices for various initial conditions revealed by dye and a horizontal light slice at the base of the convective flow: (*a*), (*b*), (*c*), and (*d*) are taken respectively at $T' \approx 4, 6, 10$ and 7, in the experiment with $N \approx 0.8\ \mathrm{s}^{-1}$, $f \approx 0.26, 0.4, 0.7$ and 1.0 s^{-1}, $B_0 \approx 2.2\ \mathrm{cm}^2\,\mathrm{s}^{-3}$ and $R_0^* \approx 0.86, 0.4, 0.20$ and 0.12. Photograph (*a*) shows the formation of a cyclonic source vortex, (*b*) shows two cyclonic vortices, (*c*) shows three cyclonic vortices, while (*d*) shows four cyclonic vortices.

the edge of the source no longer exists. Also, one can observe an anticyclone (A) near the wall of the tank. Since this anticyclone was not present in figure 4(*c*), it must have been generated by some other mechanism. To investigate the causes for such distortion in the cyclonic vortex field and the formation of the anticyclones, the

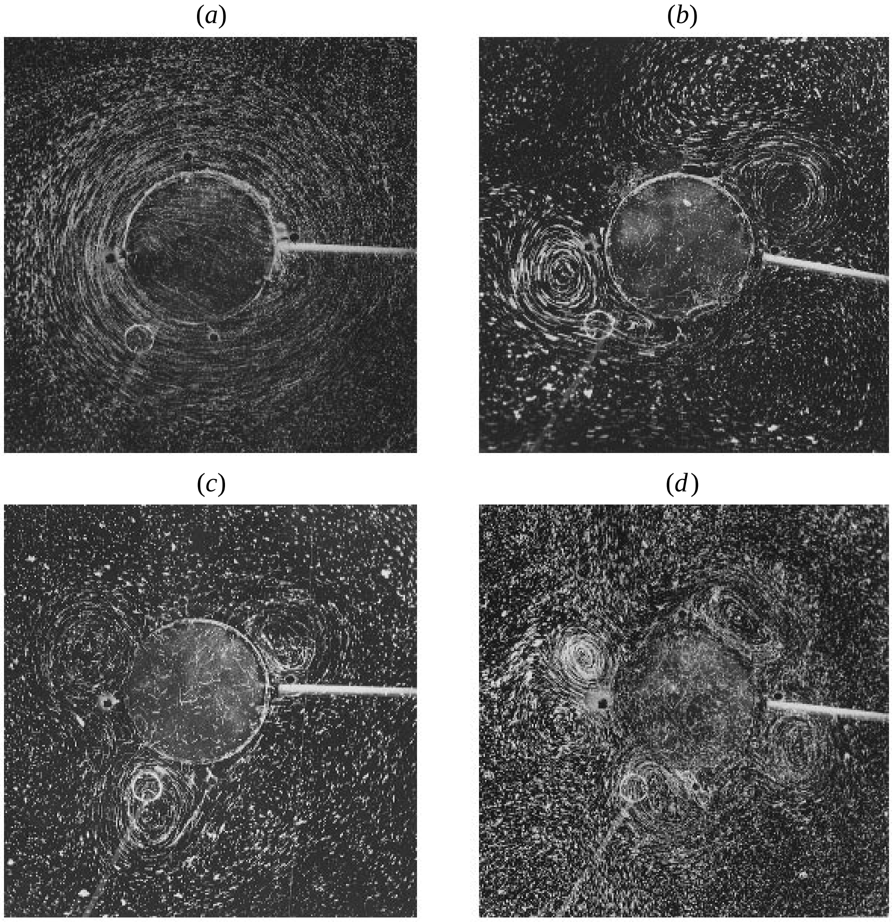

FIGURE 6. The horizontal structure of the convective cyclonic vortices near the water surface for various initial conditions as revealed by pointed streak photography (see §2) of neutrally buoyant particles. Photographs (*a*), (*b*), (*c*), and (*d*) are at $T' \approx 3, 6, 7$ and 5 for the experiment with $N \approx 0.89$ s^{-1}, $f \approx 0.25, 0.71, 1.0$ and 1.13 s—1, $B_0 \approx 2.0$ $\mathrm{cm}^2\,\mathrm{s}^{-3}$ and $R_0^* \approx 0.94, 0.39, 0.12$ and 0.098, respectively. Photograph (*a*) shows the formation of a fully developed cyclonic source vortex, while (*b*), (*c*) and (*d*) show that the number of well-organized cyclonic vortices increases with decreasing R_0^*.

method of streak photography was employed. We used two horizontal sheets of light, one placed near the surface of the water column and the other at the level of the equilibrium depth h_e. The results for the experiments where the light slice was near the surface are shown in figure 6. The photographs clearly demonstrate that all of the initially formed vortices are cyclonic and resemble those shown in figure 5 that were taken at about the same range of values of R_0^*. The results for the experiments where the light slice was located near the base of the convective flow are shown in figure 7. These photographs reveal vorticity with opposite rotation (anticyclone) when compared with figure 6, and with our previous work in homogeneous and two-layer stratified ambient fluid. We emphasize that the experiments shown in figure 6(*a*–*d*) have been conducted at about the same values of R_0^* as those shown in figure 7(*a*–*d*), respectively.

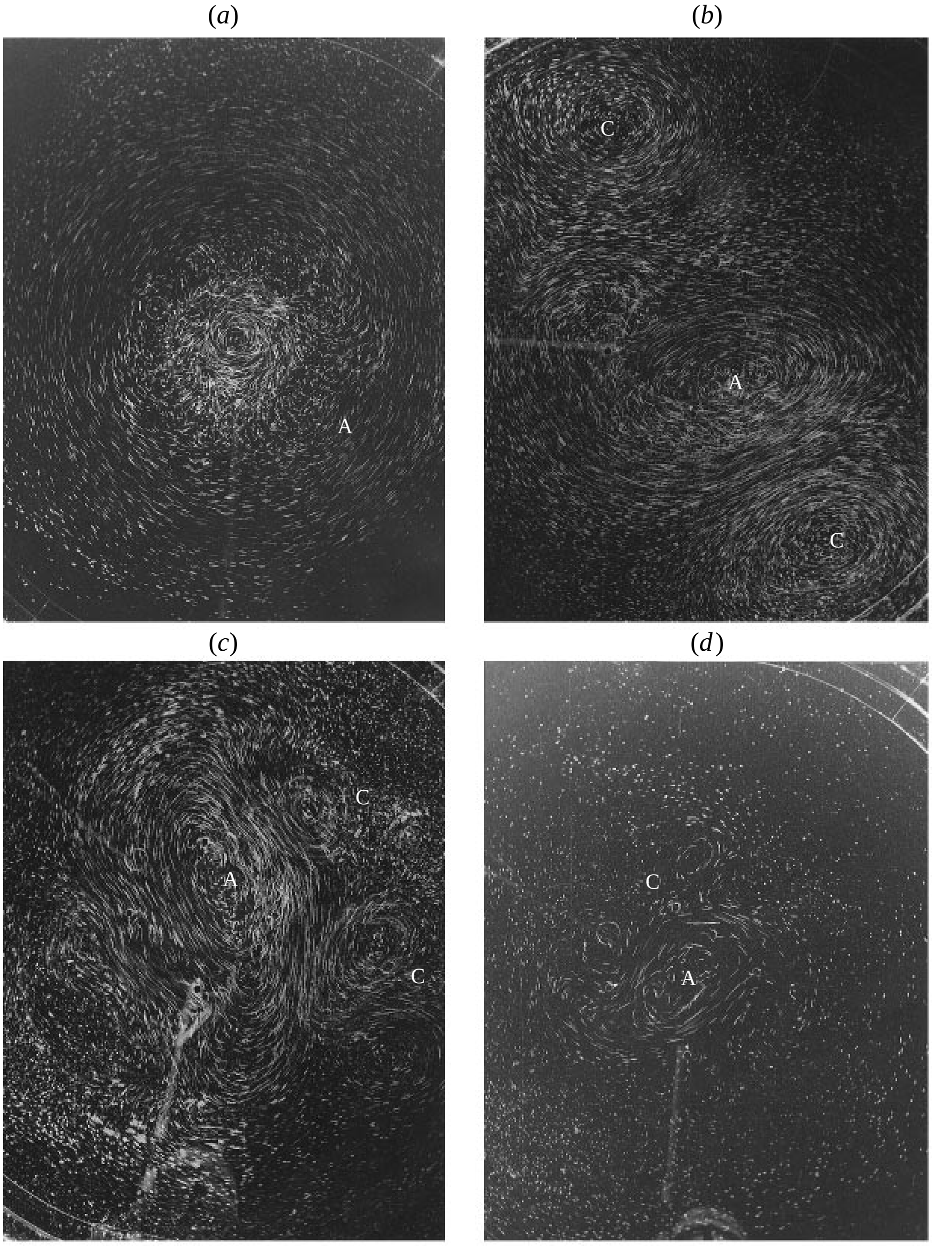

Figure 7. As in figure 6, but the structure of vortices at the base revealed here. Photographs (*a*), (*b*), (*c*) and (*d*) are at $T' \approx 3, 9, 9$ and 5, in the experiment with $N \approx 0.86\ \mathrm{s}^{-1}$, $f \approx 0.185, 0.47, 0.72$ and $0.1\,\mathrm{s}^{-1}, B_0 \approx 1.8\ \mathrm{cm}^2\,\mathrm{s}^{-3}$ and $R_0^* \approx 0.97, 0.36, 0.2$ and 0.12, respectively. Here, (*a*), (*b*), (*c*), and (*d*) present the same flow activity as shown in the dye photographs of figure 5(*a–d*), respectively. These photographs show clearly the formation of the ‘bottom anticyclones’ (A) at the base of the convective flow. The base of the cyclonic vortices (C) of figure 6, are visible in these photographs.

3.2. *The generation of ‘subsurface anticyclones’*

The persistent presence of a large anticyclone at the base of the convective flow near the level of equilibrium depth is clearly evident in the photographs shown in figure 7(*a–d*), for different values of R_0^*. Figure 6(*a*) shows the formation of a well-developed

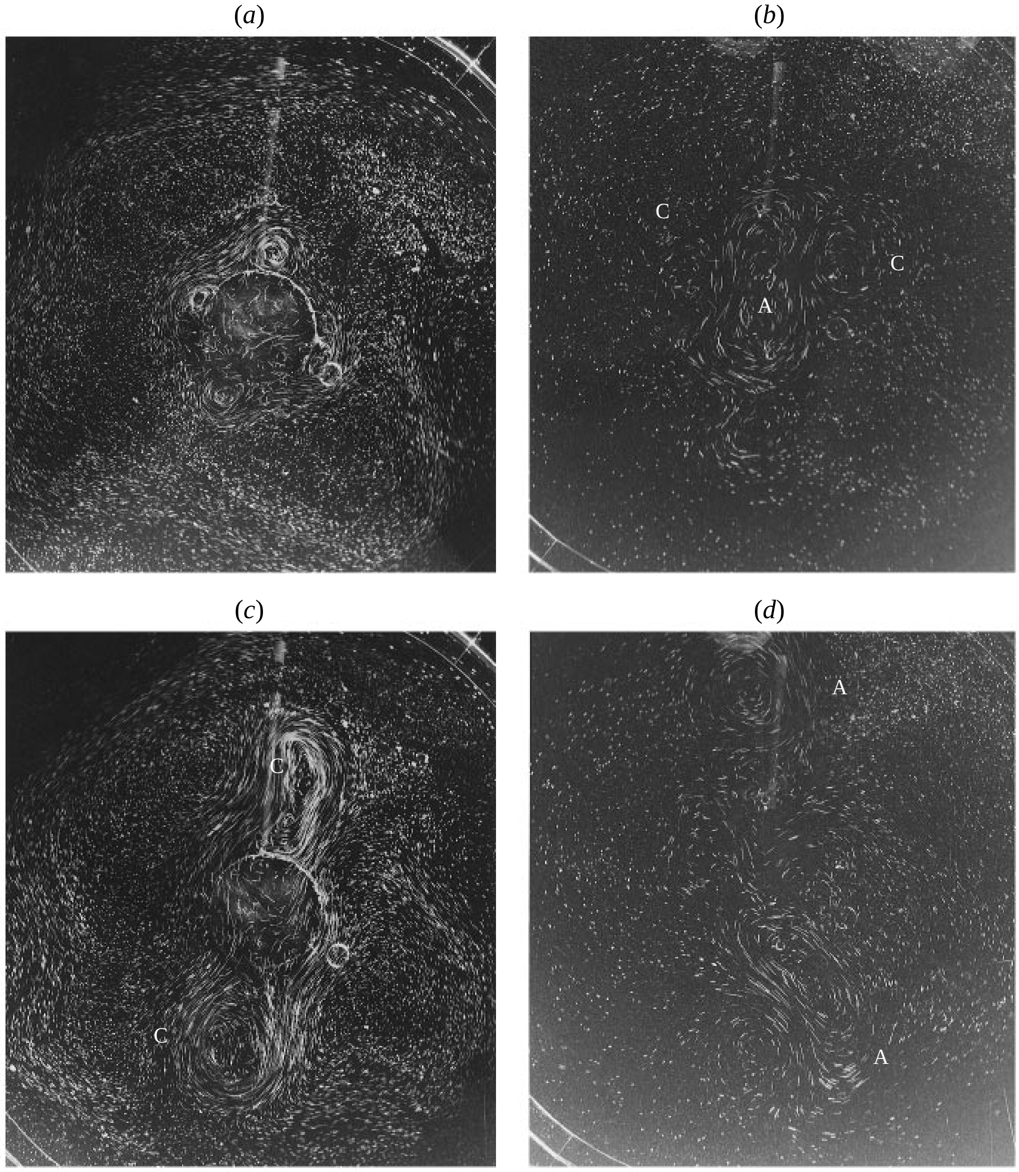

Figure 8 (*a*–*d*). For caption see facing page.

cyclonic source vortex in the upper part of the convective flow, while figure 7(*a*) shows the formation of a well-developed anticyclonic vortex near the base of the convective flow. Note that in homogeneous cases the cyclonic source vortex occupied the entire depth of the water column (Narimousa 1997). Figure 6(*b*) shows the formation of two cyclonic vortices at the top, while figure 7(*b*) shows that a large anticyclone has dominated the lower part of the convective flow forcing the two cyclones toward the wall of the tank and not allowing new cyclones to form. Figure 7(*c*) shows an elongated large anticyclone beneath the three cyclones of figure 6(*c*). A similar situation is also documented in figures 7(*d*) and 6(*d*), where initially four cyclones are formed at the top.

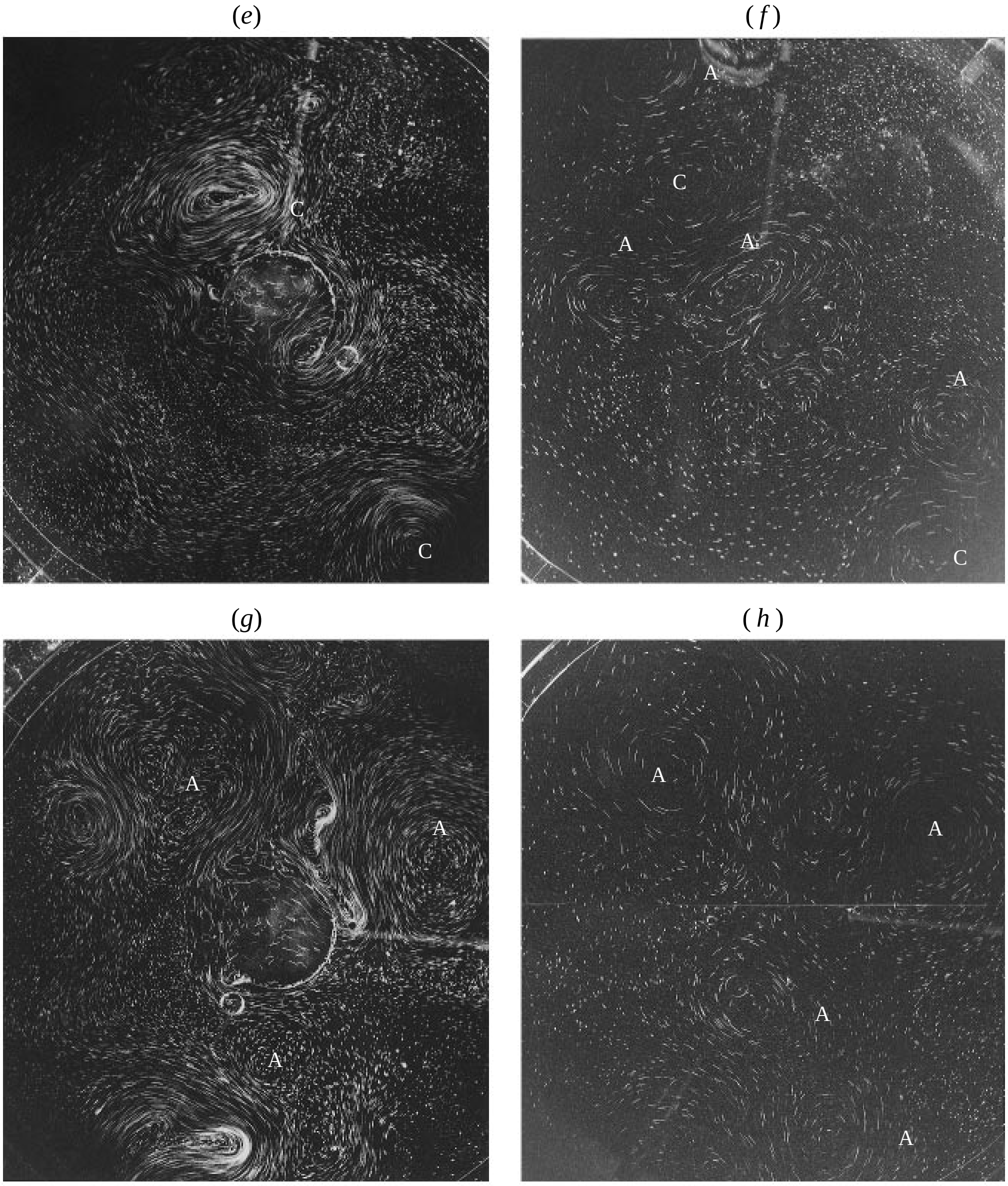

Figure 8. Successive pictures of the horizontal structure of the convective regions near the top (a, c, e, g) and the base of the convective flow (b, d, f and h) for the experiment with $N \approx 0.86$ s^{-1}, $f \approx 1.0$ s^{-1}, $B_0 \approx 1.8$ $\mathrm{cm}^2\,\mathrm{s}^{-3}$ and $R_0^* \approx 0.12$. (a) At $T' \approx 6$, showing the initial formation of four cyclonic vortices revealed near the surface of the water column. (b) At $T' \approx 6.8$, showing the presence of a large anticyclone near the base of the convective flow. This photo was taken $2T'$ after the one shown in figure 7(c). It can be seen that the anticyclone is about to split into two vortices. The base of the cyclones (C) are visible in this photo. (c) At $T' \approx 8.5$, the bottom anticyclonic instability has affected the cyclones above it and forced the cyclones to join into two vortices and take the same orientation as that of the anticyclone. (d) At $T' \approx 9.5$: here the anticyclonic instability has resulted into two anticyclones (A). (e) At $T' \approx 13$: the two cyclones are fully developed. (f) At $T' \approx 13.7$, where several anticyclones are formed in the lower part of the convective system. The bases of the two cyclones are still visible at the base of the convective flow. (g) At $T' \approx 20$, showing the structure of a well-developed convective system in linearly stratified ambient. Due to the presence of the solid wall the cyclones are still present in this photo, while the central part is dominated by the anticyclones that are now weakly visible at the top. (h) At $T' \approx 20.5$, showing the total domination of the convective system by the anticyclones.

As mentioned above, anticyclones were absent in homogeneous and two-layer stratified cases. Therefore, the generation of the bottom anticyclone in the present linearly stratified experiments must arise from a mechanism that takes place at the base of the convective flow. As discussed in §3.1 and shown in figure 3, after a rapid penetration the convective flow reaches an equilibrium depth h_e, where it begin to propagate radially in the form of a gravity front. At this stage a density interface $\delta\rho_i$ must form at the base of the mixed layer that is strong enough to hold the convective flow at depth h_e (figure 2*b*). This requires the formation of a thin intermediate layer of depth h_i at the base of the mixed convective flow. The inflow into the intermediate layer, mainly contributed from the top convective flow and partly from the entrained mixed flow from below, can only propagate radially outward in the form of a shear flow. Then, the stronger effect of rotation at larger depths (Julien *et al.* 1996) will dominate the intermediate layer which naturally forces it to rotate in an anticyclonic manner. In this way, a large 'bottom anticyclone' forms at the base of the convective flow beneath the source. Initially, the anticyclone is thin and its depth h_a is about the same as that of the intermediate layer, that is $h_a \approx h_i$, while its mean diameter is about the same size as that of the convection source itself (figure 7*d*). In the following we will see that the behaviour of the 'subsurface anticyclone' depends on the initial conditions of a given system (N, Bo, f and R).

At higher values of $R_0^* > 0.5$, a single anticyclonic source vortex was formed at the bottom and continued to grow to a large size while dominating the lower part of the convective system (figure 7*a*). Concurrently, the upper part of the system was dominated by a single cyclonic source vortex (figure 6*a*). As mentioned earlier, for the case where two cyclonic vortices were formed, the 'subsurface anticyclone' grows to a larger size, dominating the central part of the convective system and not allowing new cyclones to form (figure 7*b*). At lower values of R_0^*, initially three or more cyclonic vortices were generated in a given system. Figure 8(*a*) reveals the formation of at least four cyclonic vortices in the vicinity of the convection source near the surface of the water column. At about the same time, a large 'subsurface anticyclone' has already formed at the base of the convective flow (figure 8*b*), beneath the cyclones of figure 8(*a*). It can be seen that this anticyclone is unstable and is about to split into two anticyclones. It is evident in figure 8(*c*) that such bottom instability has influenced the cyclonic vortices of figure 8(*a*). These four cyclones are forced to coalesce into two larger vortices and to take the same orientation as that of the 'bottom anticyclone'. At the base, the anticyclone has split into two vortices (figure 8*d*). Several rotation periods later, the two cyclones are still visible in figure 8(*e*), while at least four 'bottom anticyclones' are generated in the lower part of the convective system (figure 8*f*). Eventually, after many rotation periods, the anticyclones extend throughout the convective system such that one can observe the top of these vortices in figure 8(*g*). Figure 8(*h*) shows the total domination of the convective flow by at least four anticyclonic vortices with strong presence at the base of the convective system.

In general, the evidence presented in this section indicates that deep, turbulent convection in a linearly stratified ambient fluid results in the formation of a large single 'bottom anticyclone' at the base of the convective flow. As explained above, the behaviour of this anticyclone depends on the natural Rossby number of the system R_0^*. At larger values of R_0^*, usually one large anticyclone will eventually dominate the central part of the convective system (figure 7*a*,*b*). At lower values of R_0^*, eventually several 'bottom anticyclones' will dominate the convective system (figure 8*h*).

4. Theory and scaling arguments

4.1. *The initial penetration*

As discussed in §3.1, a deep, convective three-dimensional turbulent flow was generated by a negative buoyancy flux B_0 in the top layer of a linearly stratified rotating water column of strength N (buoyancy frequency). The convective flow then penetrated rapidly into the linear stratification until it reached an equilibrium depth h_e (figure 3*b*,*c*), where it began to propagate (radially) outward from beneath the convection source. Under such circumstances, we can write

$$g_i'h_e \sim N^2h_e^2 \tag{4.1}$$

where $g_i'h_e$ is the energy required to stir the linear stratified layer of depth h_e having a buoyancy frequency N. Here, g_i' is the reduced gravity at the base of the propagating convective flow and the equilibrium depth. From (4.1), the equilibrium depth is

$$h_e = \alpha g_i'/N^2 \tag{4.2}$$

where α is a constant of proportionality to be determined experimentally.

When a penetrative convective flow reaches an equilibrium depth, a weak but sufficiently strong density jump must form at the base of the mixed layer (figure 2*b*,*c*) to hold the turbulent convective flow from further deepening due to buoyancy and entrainment forces. Under such circumstances, in a study of turbulent convection in the presence of a density interface (Narimousa 1996) we have found a critical Richardson number ($Ri_c = g'h_e/(B_0R)^{2/3}$) above which the convective flow cannot penetrate the density interface (here $g' = g_i' - g_c'$, and $g_c' \approx 10(B_0R)^{2/3}/h_e$ is the density of the convective mixed flow given in Narimousa 1997). Using this, we can write

$$Ri_c \approx (g_i' - g_c')h_e/(B_0R)^{2/3} \approx 11, \tag{4.3}$$

where $(B_0R)^{1/3}$ is the radial velocity of the outflow from under the source (Phillips 1966; Narimousa 1997). Substituting for g_i' from (4.3), the relationship (4.2) becomes

$$h_e \approx (22/\alpha)^{1/2}(B_0R)^{1/3}/N \tag{4.4}$$

which supports that given by Visbeck *et al.* (1996) and later confirmed by Whitehead *et al.* (1996). An estimate of the value of the reduced gravity g_i' at the base of the mixed layer can be estimated by substituting (4.4) in (4.2):

$$g_i' \approx (22\alpha)^{1/2}(B_0R)^{1/3}N. \tag{4.5}$$

The depth of the interfacial layer h_i can be estimated from

$$N^2 = \left(g_c' + g'\right)/\left(h_e + h_i\right). \tag{4.6}$$

Using (4.3), (4.5) and the density of the convective mixed flow $g_c' \approx 11(B_0R)^{2/3}/h_e$ from measurements of Narimousa (1996), we find

$$h_i \approx \left((22\alpha)^{1/2} - (22/\alpha)^{1/2}\right)(B_0R)^{1/3}/N. \tag{4.7}$$

In order for $h_i > 0$ to exist, it is clear from (4.7) that $\alpha > 1$ (see §5). It can be seen from (4.7) that similarly to h_e, here h_i is also independent of rotation rate f.

4.2. *The effect of rotation*

Once an equilibrium depth was reached, the convective mixed flow began to propagate radially outward (a front) from beneath the source. At this stage, similarly to the homogeneous cases, the rotational effects dominated the front and as a result mesoscale cyclonic vortices were generated around the convection source initially (figure 6). Under these circumstances, the mean diameter (D) of the cyclonic vortices should scale with the local Rossby deformation radius $L_R = Nh_e/f$ (Griffiths & Linden 1981), that is,

$$D \sim Nh_e/f. \tag{4.8}$$

Substituting for h_e from (4.4), the relationship (4.8) becomes $D \sim (B_0R)^{1/3}/f$, and/or

$$D/R \sim (R_{0,R})^{2/3}, \tag{4.9}$$

where $R_{0,R} = (B_0/f^3R^2)^{1/2}$ is the Rossby number based on the radius R of the source. The relationship (4.9) is the same as that obtained for the vortices of homogeneous cases (for details see Maxworthy & Narimousa 1994; Narimousa 1997). The swirl velocity (v) of the cyclonic vortices can be estimated from the thermal wind equation

$$fv = g'_c\delta h/\delta r. \tag{4.10}$$

Here, h is the radial (r) variation of the vortex shape and $\delta h/\delta r$ is the local vortex slope. Taking $\delta r \sim D$ and $\delta h \sim h_e$, we obtain

$$v \sim (B_0R)^{1/3}. \tag{4.11}$$

Similarly, the density g'_v within the cyclonic vortices can be estimated from

$$g'_v \approx 10(B_0R)^{1/3}/f, \tag{4.12}$$

details of which are given in Narimousa (1997).

4.3. *The 'bottom anticyclones'*

As discussed in §3.2, shortly after the formation of cyclonic vortices ($\sim 2T'$) a large, thin 'subsurface anticyclone' formed at the base of the mixed layer beneath the convection source. It was also noted that the presence of an interfacial layer at the base of the mixed layer is responsible for the formation of the 'bottom anticyclones'. This arises from the fact that the mean flow in the interfacial layer is radially outward together with the stronger influence of rotation at higher depths (Julien *et al.* 1996), and can only produce an 'anticyclone'. Initially, the thickness of the anticyclone h_a is about the same as that of the interfacial layer $h_a \approx h_i$, and its density is $g'_a \approx g'_i$. Referring to §3.2 and figure 8, the anticyclones extend throughout the mixed layer, except for large values of R_0^* where the anticyclone remains beneath the single cyclonic source vortex (figures 6*a* and 7*a*). Here, the mean diameter of the anticyclones D_a should scale with the Rossby deformation radius $L_{Ri} = (g'_ih_i)^{1/2}/f$, that is,

$$D_a \sim (g'_ih_i)^{1/2}/f. \tag{4.13}$$

Substituting for g'_i from (4.5) and h_i from (4.7) in (4.13), we find

$$D_a/R \sim (R_{0,R})^{2/3} \tag{4.14}$$

which is the same as that found for the cyclonic vortices in (4.9). The constant of proportionality for (4.9) and (4.14) will be determined experimentally (see §5). Using the thermal wind equation ($fv_a = g'_i\delta h_i/\delta r$), we find that the swirl velocity v_a within the anticyclones is estimated by

$$v_a \sim (B_0R)^{1/3}. \tag{4.15}$$

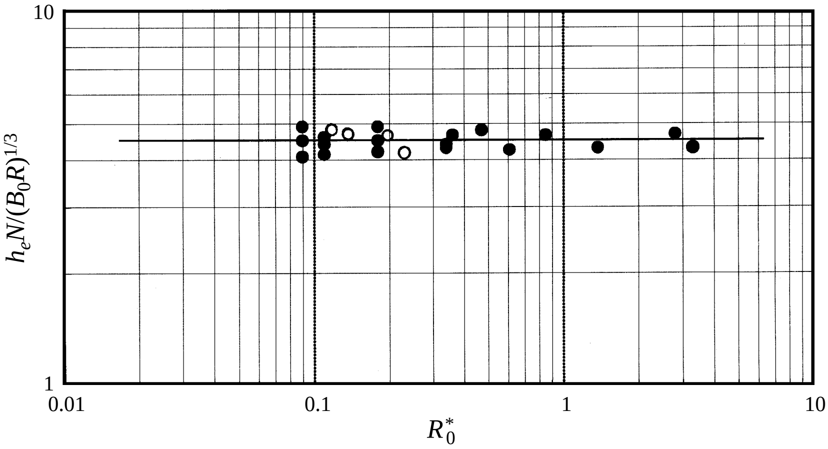

FIGURE 9. Variations of the equilibrium depth h_e normalized with $(B_0R)^{1/3}/N$, as a function of R_0^*. Open circles are taken from Ivey *et al.* (1995).

5. Experimental measurements and comparison with theory

5.1. *The equilibrium depth* (h_e)

We have measured the mean equilibrium depth h_e from photographs such as those shown in figure 3 for many different experiments with various initial conditions. In a given experiment, the measured value of h_e is normalized with $(B_0R)^{1/3}/N$ and then plotted against R_0^*, as shown in figure 9. It can be seen that the quantity $h_eN/(B_0R)^{1/3}$ is independent of R_0^* which confirms the prediction (4.4). Figure 9 yields

$$h_e \approx 4.5(B_0R)^{1/3}/N \tag{5.1}$$

which is the same as that obtained by experiments of Whitehead *et al.* (1996) and very close to that given by numerical model ($h_e \approx (3.9 \pm 0.9)(B_0R)^{1/3}/N$) of Visbeck *et al.* (1996). Figure 9 also contains the data for the same parameters taken from figure 9 of Ivey *et al.* (1995). It can be seen clearly, within the range of experimental error, that their data agree well with the present data providing further support for (5.1) (see also Visbeck *et al.* 1996).

Comparing (5.1) with (4.4) we obtain $\alpha \approx 1.08$, which is in agreement with the prediction that $\alpha > 1$ required for the validity of equation (4.7). Substituting for α in (4.2) and (4.5), we find that

$$h_e \approx 1.08(g_i'/N^2) \tag{5.2}$$

and

$$g_i' \approx 4.87(B_0R)^{1/3}N \tag{5.3}$$

where (5.3) gives an estimate of the density jump at the base of the mixed layer at the level of equilibrium depth. Knowing the initial conditions of a given system, one can estimate the value of g_i' from (5.3) and then the value of h_e from (5.2). It can be seen that h_e can be estimated either directly from (5.1) and/or combination of (5.3) and (5.2).

Knowing α, an estimate of the depth of the interfacial layer h_i from (4.7) is given by

$$h_i \approx 0.36(B_0R)^{1/3}/N \tag{5.4}$$

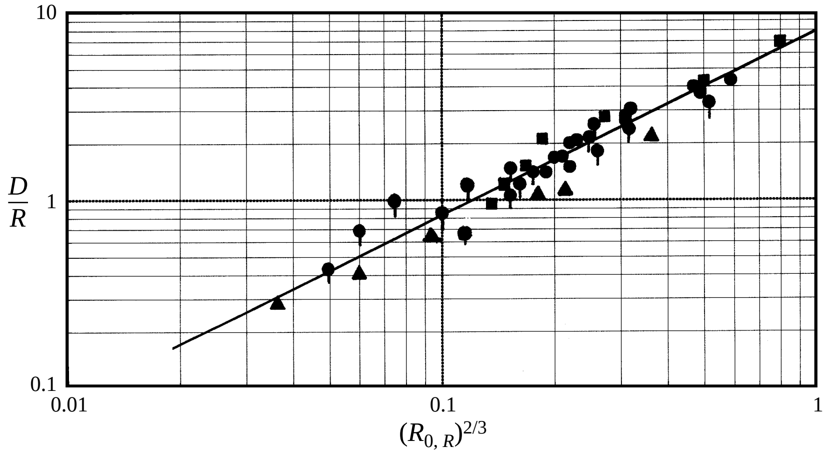

FIGURE 10. Variations of the mean diameter D of the cyclonic vortices with $R_{o,R}$. The various symbols represent the data from the present study (●), Narimousa (1996) (■), Narimousa (1997) (⫯), and Jones and Marshall (1993) (▲). Note that the slope of the solid line is about 1.

which yields the ratio

$$h_i/h_e \approx 0.08. \tag{5.5}$$

As expected, the depth of the interfacial layer h_i is much smaller ($\sim$ 8%) than the depth h_e of the overlaying mixed layer itself.

5.2. *Diameter of the cyclonic vortices* (D)

Initially, as described in §4.2 and demonstrated in figure 8, cyclonic vortices form around the convection source in a manner similar to the homogeneous (Maxworthy & Narimousa 1994; Narimousa 1997) and two-layer stratified (Narimousa 1996) cases. As in those experiments, here also we have measured the maximum mean diameter D of the fully developed cyclonic vortices from the photographs such as the one shown in figure 8. The values of D/R as a function of $(B_0R)^{2/3}$, according to the relationship (4.9), are plotted in figure 10. It can be seen that the present data indicated by solid circles (●) support the prediction (4.9) and yields

$$D/R \approx 8(B_{0,R})^{2/3}. \tag{5.6}$$

Figure 10 also includes the data from homogeneous cases (Narimousa 1997), two-layer stratified cases (Narimousa 1996), and the numerical model of Jones & Marshall (1993). Within the range of experimental errors, figure 10 demonstrates that the maximum mean diameter of the mesoscale cyclonic vortices is clearly given by (5.6), which is independent of the ambient fluid and the surface (solid or free) that the vortices are generated on.

5.3. *Cyclonic vortex velocity* (v)

Using photographs such as those shown in figure 6, we have measured the maximum swirl velocity (v) within the cyclonic vortices, normalized it with $(B_0R)^{1/3}$, and shown it in figure 11 as a function of their associated value of R_0^e. It can be seen that the data in figure 11 support the prediction (4.11) and provide

$$v \approx (B_0R)^{1/3} \tag{5.7}$$

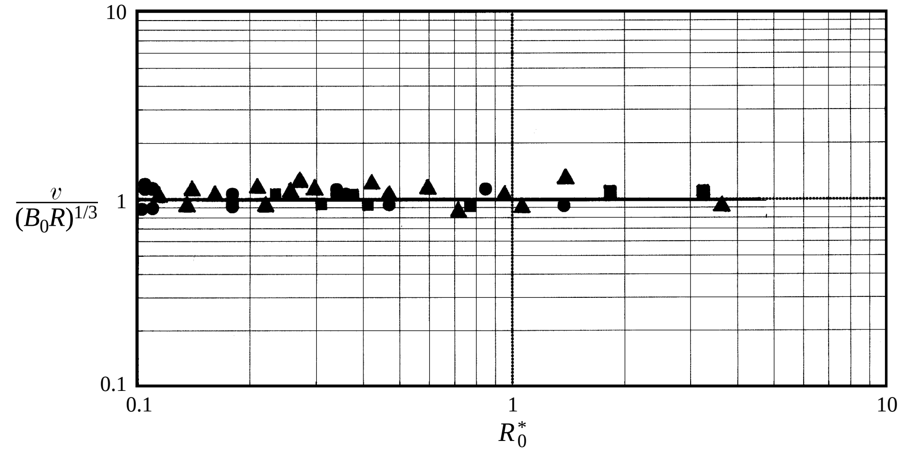

FIGURE 11. Variations of the maximum swirl velocity v of the cyclonic vortices normalized with $(B_0R)^{1/3}$, as a function of R_0^*. The various symbols represent the data from the present study (●), Narimousa (1996) (■), and Narimousa (1997) and Maxworthy & Narimousa (1993) (▲).

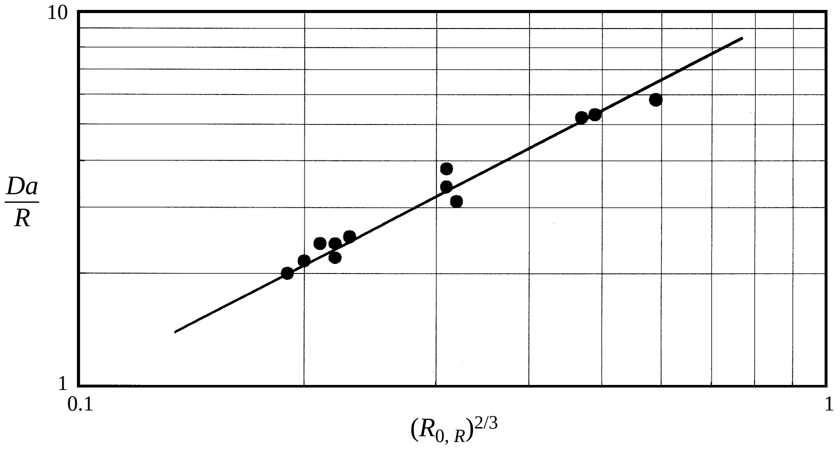

FIGURE 12. Variations of the mean diameter D_a of the anticyclonic vortices normalized with R, as a function of $R_{0,R}$. Note that the slope of the solid line is about 1.

which is the same as that found in the homogeneous (Narimousa 1997) and two-layer stratified cases (Narimousa 1996). The data from those experiments have also been included in figure 11. Figure 11 demonstrates that the maximum swirl velocity v is given by (5.7), which is independent of the ambient fluid and the surface (solid or free) that the vortices are generated on.

5.4. *Diameter of the 'subsurface anticyclonic vortices' (D_a)*

As demonstrated in figure 8, after about two rotation periods a thin ($\sim h_i$) 'bottom anticyclone' with a size comparable to that of the source itself ($\sim R$) forms at the level of equilibrium depth beneath the convection source. The anticyclones generated then continue to grow, both vertically and radially. When these vortices reach a maximum size, we measured their mean diameter and have plotted the results in figure 12 according to the relationship (4.14). The data in figure 12 supports the prediction

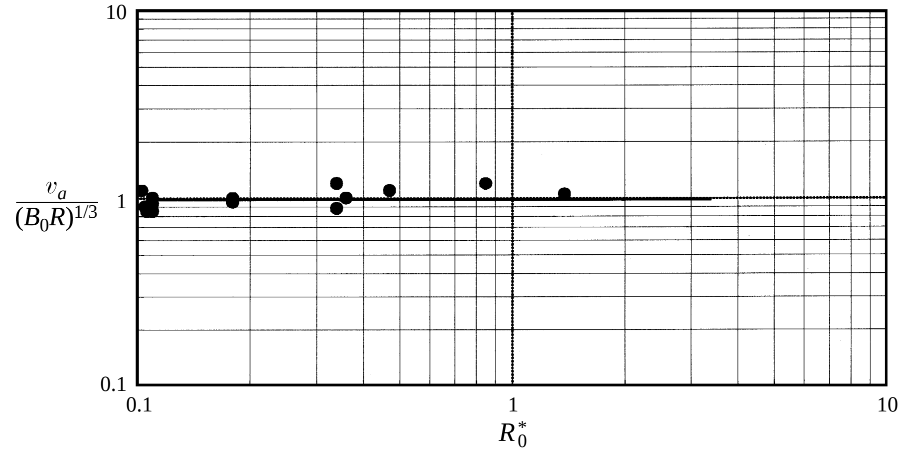

FIGURE 13. Variations of the maximum swirl velocity (v_a) of the bottom anticyclonic vortices normalized with $(B_0R)^{1/3}$, as a function of R_0^*.

(4.14) and yields

$$D_a/R \approx 10(B_{0,R})^{2/3}. \tag{5.8}$$

Comparing (5.8) with (5.6) we find that $D/D_a \approx 0.8$, indicating that the 'bottom anticyclones' are larger ($\sim$ 20%) than the cyclonic vortices.

5.5. *Anticyclonic vortex velocity* (v_a)

Using photographs such as those shown in figure 7, we have measured the maximum horizontal velocity v_a within the anticyclonic vortices, normalized it with $(B_0R)^{1/3}$ and then plotted the results against the associated value of R_0^*, as shown in figure 13. The data in figure 13 supports the prediction (4.15) and gives

$$v_a \approx (B_0R)^{1/3} \tag{5.9}$$

which is the same as that found in (5.7) for the cyclonic vortices. The relationships (5.7) and (5.9) clearly demonstrate that the value of the maximum swirl velocity of both the cyclones and anticyclones depends only on the characteristics of the forcing region.

6. Geophysical applications

6.1. *The central Arctic Ocean*

In the upper central Arctic Ocean, the stratification usually consists of a top mixed layer of about 35 m depth, with a moderately sharp density jump at its base followed by a stratified layer of lower stability beneath, sometimes called the 'pycnocline', that extends to a depth of about 300 m (Newton *et al.* 1974; Hunkins 1974). This stratified system rests on top of a nearly homogeneous water column that then extends to great depths (2000–4000 m). In the two-layer stratified experiments of Narimousa (1996), we have found that when $Ri < 11$, the convective flow will eventually penetrate through the density interface and into the bottom layer. Based on the total density jump across the stratified layer (pycnocline) with $g' \approx 4$ cm s^{-2} at an average depth of about $h_0 \approx 125$ m, we find that $Ri \approx 50$ (where $B_0 = 3 \times 10^{-3}$ cm^2 s^{-3} and

$R = 100$ km). Since the value of $Ri \approx 50$ found here is much larger than 11, we anticipate that the three-dimensional convective flow will not penetrate into the deep Arctic.

However, if we consider the initial density jump at the base of the mixed layer (or top of the pycnocline) with $g' \approx 1$ cm s^{-2} and $h_0 \approx 50$ m, we find that $Ri \approx 5.2$, which is considerably smaller than 11, indicating that the three-dimensional convective flow will penetrate through the initial density jump and into the stratified pycnocline itself, creating a situation similar to the present study. Taking $N \approx 10^{-2}$ s^{-1} for the stratification across the pycnocline, we estimate from (5.1) the equilibrium depth $h_e \approx 150$ m for the central Arctic Ocean. That is, we predict that the convective mixed flow will penetrate a total depth of about 200 m to reach its equilibrium depth and then propagate radially inside the pycnocline of the Arctic. It is in this region of the Arctic (the pycnocline), as mentioned in §1, where a large number of subsurface (more than 100) mesoscale vortices have been detected, the majority of which are anticyclones. These vortices, detected in depths 50–300 m, have a central core of about 10–20 km, a thickness of about 100 m, and velocities on the order of 30 cm s^{-1}. Using the estimated value of the equilibrium depth as 200 m and $f \approx 1.4 \times 10^{-3}$ s^{-1}, we estimate that $R_0^* \approx 1.65$ for the convective system in the upper central Arctic Ocean. Then according to the present study (as demonstrated in §3.2), at least one 'subsurface anticyclone' should form at the base of the convective flow inside the pycnocline. In fact, as far as we are aware, the present work is the first physical evidence that directly demonstrates the generation of 'subsurface anticyclones' in convective systems that occur in a stratified ambient fluid. Using (5.8) and (5.9), we estimate the mean diameter $D \approx 21$ km and swirl velocity $v_a \approx 31$ cm s^{-1} for the anticyclonic vortices in the upper layer of the central Arctic Ocean. These predictions are in excellent agreement with the field values, and with the fact that the 'anticyclones' form inside the pycnocline as reported by Newton *et al.* (1974), among others.

6.2. *The Labrador Sea*

Unlike the upper layers of the central Arctic Ocean, the stratification in the Labrador Sea is weak and, according to the data presented by Lazier (1994), the buoyancy frequency is about $N \approx 10^{-3}$ s^{-1}. Using the typical field values ($B_0 \approx 3 \times 10^{-3}$ cm^2 s^{-3}, $f \approx 1.4 \times 10^{-4}$ s^{-1} and $R \approx 100$ km) for intense convection (Lazier 1980) in the Labrador Sea, we estimate the equilibrium depth $h_e \approx 1390$ m for the convective mixed layer. This estimate is very close to that (1262 m) predicted by Whitehead *et al.* (1996) for winter of 1972 with heat fluxes reaching 800 W m^{-2} and the depth of the mixed layer reaching 1500 m. Using this value of h_e, we estimate that $R_0^* \approx 0.24$ which suggests that at least three cyclonic vortices with diameter of about $D \approx 16$ km (equation (5.6)) should form initially around the convection source in the Labrador Sea. As demonstrated in §3.2, a 'subsurface anticyclone' with diameter of about $D_a \approx 21$ km (equation (5.8)) should form at the base of the mixed layer. Also, as shown in figure 8, during the course of a convective event with $R_0^* \approx 0.24$, several 'subsurface anticyclones' should be generated in the deep Labrador Sea. Finally, from (5.7) and (5.9) we estimate the value of the swirl velocity $v \approx v_a \approx 31$ cm s^{-1} for the cyclones and the anticyclones of the Labrador Sea.

7. Summary and conclusions

Penetrative turbulent convection into linearly stratified ambient fluid has been investigated in a rotating laboratory tank. The turbulent convective flow generated from a localized circular top surface penetrated rapidly into the stratified water layer until it reached an equilibrium depth h_e, where further penetration due to buoyancy was arrested (figure 3). At this stage, the convective flow began to propagate radially at the level of the equilibrium depth, allowing the formation of baroclinic cyclonic vortices in the vicinity of the convection source (figure 6). Soon after, a large 'subsurface anticyclonic' vortex was formed at the base of the convective flow beneath the convection source. In the following we summarize the most important results of the present study.

(*a*) As far as we are aware, the present study has revealed the first physical evidence that demonstrates directly the generation of 'subsurface anticyclones' that are induced as a result of large-scale convection in linearly stratified ambient. Using equations (5.8) and (5.9), we have estimated the mean diameter $D_a \approx 21$ km and the maximum swirl velocity $v_a \approx 31\,\mathrm{cm\,s^{-1}}$ for the anticyclonic vortices in the upper layers of the central Arctic Ocean. These predictions are in an excellent agreement with the observed values (see §6.1). Furthermore, our model (see §6.1) predicts an equilibrium depth $h_e \approx 200\,\mathrm{m}$, which is well inside the pycnocline of the Arctic Ocean, implying that the vortices of the Arctic should form inside its pycnocline as measured and reported by (Newton *et al.* 1974; Hunkins 1974; Manley & Hunkins 1985 and D'Asaro 1986). Therefore, we conclude that the model presented in this paper has revealed strong evidence that the 'subsurface anticyclonic' vortices in the upper layers of the Arctic Ocean are generated as a result of turbulent convection inside the stratified pycnocline of the Arctic itself.

Similar predictions have also been made (see §6.2) for the convective events in the Labrador Sea which can be compared to field observations when they become available. Note that several cruises are supported by various US Federal agencies to study convective events in the Labrador Sea in considerably greater detail.

(*b*) A weak but sufficiently strong density interface must form at the base of the convective flow at the level of equilibrium depth to arrest further penetration due to buoyancy and turbulent entrainment forces. The required values of density interface g_i' and its thickness h_i can be estimated from (5.3) and (5.4), respectively. The formation of such an interfacial layer was absent in the homogeneous (Maxworthy & Narimousa 1994; Narimousa 1997) and two-layer cases (Narimousa 1996), and no anticyclone was observed in those experiments. Therefore, following the reasons given in §3.2, we conclude that the presence of such an interfacial layer at the level of equilibrium depth is responsible for the formation of the 'subsurface anticyclones'.

(*c*) Initially, cyclonic vortices form around the convection source but as demonstrated in §3.2 (figure 8), the formation of 'subsurface anticyclones' will eventually dominate the central part of the convective system by breaking the usual well-organized cyclonic vortex pattern observed in our previous work (Maxworthy & Narimousa 1994; Narimousa 1996, 1997). As a result, no new cyclones were induced in the system while the initially generated cyclonic vortices continued to grow toward their maximum size. Measurements of the maximum mean diameter D and swirl velocity v of the cyclonic vortices produced the same results ((5.6) and (5.7)) as in the above-mentioned two-layer and homogeneous cases. Therefore, within the range of experimental errors, we conclude that the maximum mean diameter D and the swirl velocity v of the mesoscale cyclonic vortices induced in a convective system are given by (5.6) and (5.7), and are independent of the ambient stratification and the surface (solid and free) that these vortices are generated on. Also, since $v \approx v_a$, we conclude that the swirl velocity of the mesoscale cyclonic and anticyclonic vortices generated in a convective system have the same values.

We wish to thank the Office of Naval Research (Grant No. 0014-93-1-0489) and the National Science Foundation (Grant opp-920-7822) for supporting this work. Also, many thanks to an anonymous referee for a detailed, constructive review of the paper.

REFERENCES

Coates, M. J., Ivey, G. N. & Taylor, J. R. 1995 Unsteady, turbulent convection into a rotating, linearly stratified fluids: Modeling deep convection. *J. Phys. Oceanogr.* **25**, 3032–3050.

D'Asaro, E. A. 1988 Generation of sub-mesoscale vortices: A new mechanism. *J. Geophys. Res.* **93**, 6635–6693.

Gascard, J. C. 1978 Mediterranean deep water formation – baroclinic instabilities and oceanic eddies. *Oceanol. Aeta* 315–330.

Gascard, J. C. 1991 Open ocean convection and deep water formation revisited in the Mediterranean, Labrador, Greenland and Weddell Seas. In *Deep Convection and Deep Water Formation in the Oceans* (ed. P. C. Chu & J. C. Gascard), pp. 157–182. Elsevier

Griffiths, R. W. & Linden, P. F. 1981 The stability of vortices in a rotating, stratified fluid. *J. Fluid Mech.* **105**, 283–316.

Hart, J. E. & Killworth, P. D. 1976 On open ocean baroclinic instability in the Arctic. *Deep-Sea Res.* **23**, 637–645.

Hunkins, K. L. 1974 Subsurface eddies in the Arctic Ocean. *Deep-Sea Res.* **21**, 1017–1033.

Ivey, G. N., Taylor, J. & Coates, M. 1995 Convectively driven mixed layer growth in a rotating, stratified fluid. *Deep-Sea Res.* **42**, 331–349.

Jones, H. & Marshall, J. 1993 Convection with rotation in a neutral ocean: A study of deep-ocean convection. *J. Phys. Oceanogr.* **23**, 1009–1039.

Julien, K., Legg, S., McWilliams, J. & Werne, J. 1996 Penetrative convection in rapidly rotating flows: preliminary results from numerical simulations. *Dyn. Atmos. Oceans* **24**, 237–249.

Lazier, J. R. N. 1980 Oceanographic conditions at ocean weather ship Bravo, 1964-1974. *Atmosphere-Ocean* **18**, 227–238.

Lazier, J. R. N. 1994 The salinity decrease in the Labrador sea over the past thirty years. In *Natural Climate Variable on Decade-to-Century Time Scales.* US National Research Council.

Manley, T. O. & Hunkins, K. L. 1985 Mesoscale eddies of the Arctic Ocean. *J. Geophys. Res.* **70**, 4911–4930.

Maxworthy, T. & Narimousa, S. 1991 Vortex generation by convection in a rotating fluid. *Ocean Modelling* **92**, 1037–1040.

Maxworthy, T. & Narimousa, S. 1994 Unsteady turbulent convection into a homogeneous rotating fluid, with oceanographic applications. *J. Phys. Oceanogr.* **24**, 865–887.

MEDOC Group 1970 Observations of formation of deep water in the Mediterranean Sea, 1969. *Nature* **227**, 1037–1040.

Narimousa, S. 1996 Penetrative, turbulent convection into a rotating two-layer fluid. *J. Fluid Mech.* **321**, 299–313.

Narimousa, S. 1997 Dynamics of meso-scale vortices generated by turbulent convection at large aspect ratios. *J. Geophys. Res.* **102**, 5615–5624.

Newton, J. L., Aagaard, K. & Coachman, L. K. 1974 Baroclinic eddies in the Arctic Ocean. *Deep-Sea Res.* **21**, 707–719.

Phillips, O. M. 1966 On turbulent convection currents and the circulation of the Red Sea. *Deep-Sea Res.* **13**, 1149–1160.

Schott, F. & Leaman, K. D. 1991 Observation with moored acoustic doppler current profiles in the convection regime in the Golfe du Lion. *J. Phys. Oceanogr.* **921**, 558–574.

Schott, F. A., Visbeck, M. & Send, U. 1993 Open ocean deep convection, Mediterranean and Greenland Seas. *Ocean Processes on Climate Dyn.* **C149**, 203–225.

Visbeck, M., Marshall, J. &. Jones, H. 1996 Dynamics of isolated convective regions in the ocean. *J. Phys. Oceanogr.* **26**, 1721–1734.

Whitehead, J. A., Marshall, J. & Hufford, G. E. 1996 Localized convection in rotating stratified fluid. *J. Geophys. Res.* **101** (C11), 25705–25721.